Calcium Green FlAsH as a genetically targeted small-molecule calcium indicator

Oded Tour[1,2], Stephen R Adams[2], Rex A Kerr[3,4,8], Rene M Meijer[5], Terrence J Sejnowski[1,3–5], Richard W Tsien[6] & Roger Y Tsien[1,2,7]

Intracellular Ca^{2+} regulates numerous proteins and cellular functions and can vary substantially over submicron and submillisecond scales, so precisely localized fast detection is desirable. We have created a ~1-kDa biarsenical Ca^{2+} indicator, called Calcium Green FlAsH (CaGF, 1), to probe [Ca^{2+}] surrounding genetically targeted proteins. CaGF attached to a tetracysteine motif becomes ten-fold more fluorescent upon binding Ca^{2+}, with a K_d of ~100 μM, <1-ms kinetics and good Mg^{2+} rejection. In HeLa cells expressing tetracysteine-tagged connexin 43, CaGF labels gap junctions and reports Ca^{2+} waves after injury. Total internal reflection microscopy of tetracysteine-tagged, CaGF-labeled α_{1C} L-type calcium channels shows fast-rising depolarization-evoked Ca^{2+} transients, whose lateral nonuniformity suggests that the probability of channel opening varies greatly over micron dimensions. With moderate Ca^{2+} buffering, these transients decay surprisingly slowly, probably because most of the CaGF signal comes from closed channels feeling Ca^{2+} from a tiny minority of clustered open channels. With high Ca^{2+} buffering, CaGF signals decay as rapidly as the calcium currents, as expected for submicron Ca^{2+} domains immediately surrounding active channels. Thus CaGF can report highly localized, rapid [Ca^{2+}] dynamics.

Selective activation of distinct cellular functions is often achieved through localization of calcium signals to regions ranging in size from tens of nanometers (nanodomains) to micrometers (microdomains). Local calcium signaling is especially prominent at presynaptic active zones and postsynaptic densities—structures that are distinguished by highly organized macromolecular arrays that yield precise spatial arrangements of calcium signaling proteins[1].

Fluorescence imaging is a major tool for studying micrometer-scale local Ca^{2+} signals[1,2], but nanodomains cannot be directly resolved by light microscopy. Even on the microdomain scale, bulk cytosolic calcium, [Ca^{2+}]$_c$, as measured by diffusely distributed indicators, often fails to correlate quantitatively with biological responses such as exocytosis or channel gating that have been assumed to be [Ca^{2+}]$_c$-regulated[3,4]. One can postulate either that the relevant local intracellular calcium concentration [Ca^{2+}]$_i$ is very different from the spatially averaged concentration[5], or that molecular mechanisms other than [Ca^{2+}]$_c$ also have major roles[4,6]. Because of such controversies, much effort has been put into experimental[7–9] and theoretical[3,6,10,11] studies of localized intracellular calcium. These studies predict that the local [Ca^{2+}]$_c$ within nanometers of the mouths of Ca^{2+} channels (Ca^{2+} microdomains) is orders of magnitude larger and faster decaying than the volume-averaged [Ca^{2+}]$_c$ measured by traditional indicators distributed throughout the cytosol. One debate concerns whether a given
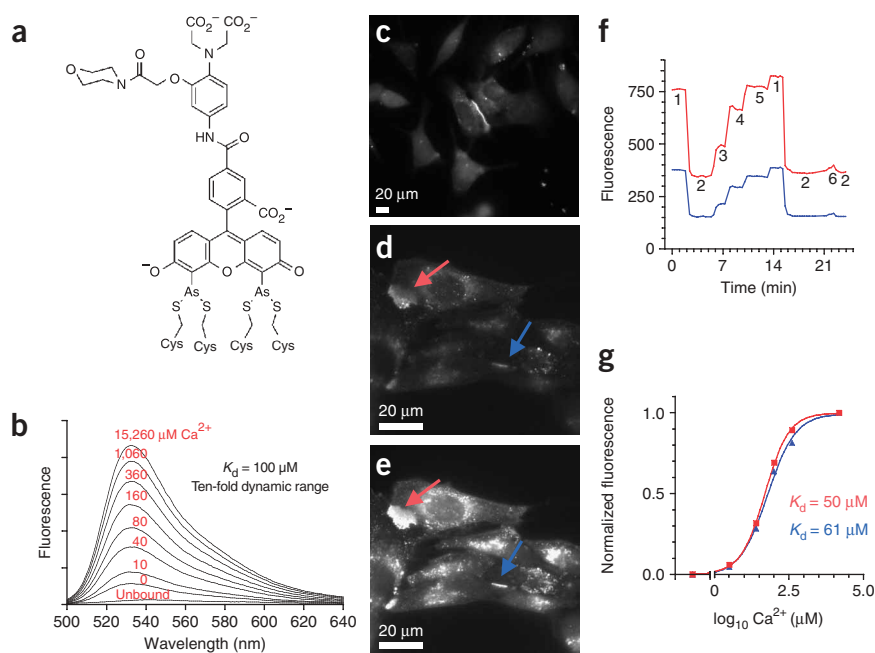
vesicle is predominantly triggered by Ca^{2+} from one local channel[12] or rather from a more widespread microdomain resulting from the superposition of the Ca^{2+} contributions of several nearby channels[13]. Experimental measurement of localized [Ca^{2+}]$_c$ has been difficult and indirect even with high-resolution imaging[14–17]. As long as the indicator is diffusely distributed, fundamental barriers of limited optical resolution will prevent measurements with the required submicroscopic spatial resolution, and consequently there is a need for new techniques that can probe calcium nanodomains.

One way to circumvent the limited spatial resolution of light microscopy is to specifically attach a calcium indicator to a target protein. The recombinant photoprotein aequorin was the first calcium indicator to be genetically targeted to specific compartments, including the mitochondria[18], nucleus[19], endoplasmic reticulum[20] and plasma membrane[8]. However, technical limitations, including low levels of luminescence and the destruction of aequorin by Ca^{2+}, complicate aequorin measurements and prevent single-cell imaging and high time-resolution comparison with electrophysiology.

Another approach is to use genetically targeted fluorescent protein–based sensors of Ca^{2+} such as the cameleons[21]. Cameleons are chimeric proteins consisting of cyan and yellow mutants of green fluorescent protein (GFP), separated by calmodulin (CaM), and the CaM-binding domain of myosin light chain kinase (M13); changes in

Figure 1 *In vitro* and intracellular titration of CaGF fluorescence. (**a**) Structure of CaGF bound to a tetracysteine-containing peptide or protein. (**b**) *In vitro* calibration of CaGF; fluorescence increased ~ten-fold (concentration is indicated in red above the traces). (**c**) A large gap junction between two HeLa cells expressing recombinant connexin 43 tagged with a tetracysteine in its C terminus and stained with CaGF. (**d–g**) Intracellular calibration of CaGF bound to cx43-GFP-C4. A field of cells with an en-face and a perpendicular gap junction (red and blue arrows, respectively) bathed in zero calcium plus 1 mM EGTA (**d**); the same field in 15 mM calcium (**e**); raw data of CaGF titration (**f**). The calcium concentrations are indicated by numbers: 1 = 15 mM; 2 = zero calcium plus 1 mM EGTA; 3 = 25 μM; 4 = 100 μM; 5 = 400 μM and 6 = nominal zero estimated at 3 μM. (**g**) Dose-response curves constructed from the data shown in **f** (red, $K_d = 50$ μM; blue, $K_d = 61$ μM).

fluorescence resonance energy transfer (FRET) between CFP and YFP give a ratiometric readout of Ca^{2+}. Recently improved cameleons[22,23] have a larger dynamic range and a substantial reduction in their sensitivity to endogenous calmodulin, both of which improve the performance of cameleons targeted to the cell membrane. However, cameleons do have intrinsic limitations. At 650 amino acids in size, the cameleons are often bigger than the host protein to which they are fused. In addition, their dynamic response is often slower than the physiological calcium signals they are supposed to report. A troponin-based indicator with a relatively fast off-rate response to Ca^{2+} was recently reported[24], but its off-rate is fitted by a double exponential decay with τ's of 142 ms and 867 ms, which are still more than two orders of magnitude slower than a typical small-molecule calcium indicator. Recently, GCaMP2, another calmodulin-based fluorescent protein-based sensor of Ca^{2+}, was tethered to Na^+ pumps to report subplasmalemmal Ca^{2+} signals on timescales of minutes[25]. However, millisecond Ca^{2+} transients within nanometers of Ca^{2+}-handling proteins have eluded direct experimental measurement.

The genetic targetability of biarsenical dyes can be combined with the fast kinetics and small size of organically synthesized calcium indicators by tagging the protein of interest with a very small peptide domain containing a tetracysteine motif[26–28], which is then labeled *in situ* with a new biarsenical Ca^{2+} indicator. In particular, we tag connexin 43, the building block of gap junctions, and the α_{1C} L-type voltage-gated calcium channel and label these proteins in living intact cells with CaGF.

RESULTS
Chemical properties of CaGF and tests on connexin 43
Calcium Green (**2**) is a hybrid between 1,2-bis(*o*-aminophenoxy) ethane-*N,N,N',N'*-tetraacetic acid (BAPTA; **3**) and fluorescein (**4**)[29] in which Ca^{2+} binding to the BAPTA inhibits photoinduced electron transfer quenching of the fluorescein. FlAsH (**5**) is a fluorescein with two arsenic substituents such that binding of a tetracysteine motif to the arsenics likewise inhibits photoinduced electron transfer quenching of the fluorescein[26]. Therefore we designed Calcium Green FlAsH as a triple hybrid combining a fluorescein with biarsenical substituents

and a BAPTA-like chelator (**Fig. 1a**; see **Supplementary Methods** online for CaGF synthesis): the upper domain provides the Ca^{2+} binding site, the middle fluorescein structure is the fluorophore, and the bottom domain contains two arsenic atoms that form four covalent bonds with the two pairs of cysteines of the tagged peptide and thereby provide genetic targetability. Because we anticipated the need to measure very rapid Ca^{2+} transients of 10s to 100s of μM, we derived the Ca^{2+} binding site from the low-affinity, pentadentate chelator *o*-aminophenol-*N,N,O*-triacetic acid (APTRA; **6**)[30] instead of octadentate BAPTA. To improve the $Ca^{2+}:Mg^{2+}$ selectivity of APTRA, we amidated one of its carboxylates with a variety of primary and secondary amines to produce new, low-affinity (20–400 μM K_d) Ca^{2+} chelators with minimal affinity ($K_d >$ 10 mM) for Mg^{2+} (data not shown). The most promising chelator containing a morpholine amide was conjugated with carboxy-FlAsH (**7**) to give CaGF. As expected, CaGF fluorescence is highly quenched when the dye is not bound to a tetracysteine peptide. Peptide binding increases the fluorescence by greater than four-fold, after which Ca^{2+} binding enhances the fluorescence a further ten-fold with a $K_d = 100$ μM for Ca^{2+} (**Fig. 1b**). The rate constants for Ca^{2+} binding were too high to easily resolve experimentally, but using a stopped-flow apparatus, we determined that the off-rate was above 2,000 s^{-1} (**Supplementary Methods**). This is consistent with $> 20,000$ s^{-1} off-rates of structurally similar calcium-binding molecules with comparable K_d's[31].

To test CaGF in living cells, it was necessary to generate an AM ester derivative of CaGF because the multiple carboxylates render CaGF less membrane permeable than FlAsH or ReAsH (**8**)[27]. The CaGF/AM (**9**) penetrates living cells, and after esterase cleavage it is able to bind the target protein. To test the specificity of CaGF, we expressed in HeLa cells a recombinant connexin 43 tagged with a tetracysteine motif in its C terminus (cx43-TC). Connexin 43 is tightly localized to gap junctions, and CaGF staining of these cells showed strong fluorescence in gap junctions between cells (**Fig. 1c**). We also used a connexin 43 tagged with Emerald GFP and an optimized tetracysteine peptide[32] (cx43-GFP-C4), with the GFP serving as both an internal fluorescent marker for recombinant protein expression and a reference signal to estimate the completeness of labeling of CaGF. To test the calcium sensitivity, we expressed cx43-GFP-C4 in cells, briefly fixed the cells with 3% paraformaldehyde to prevent motility, permeabilized them
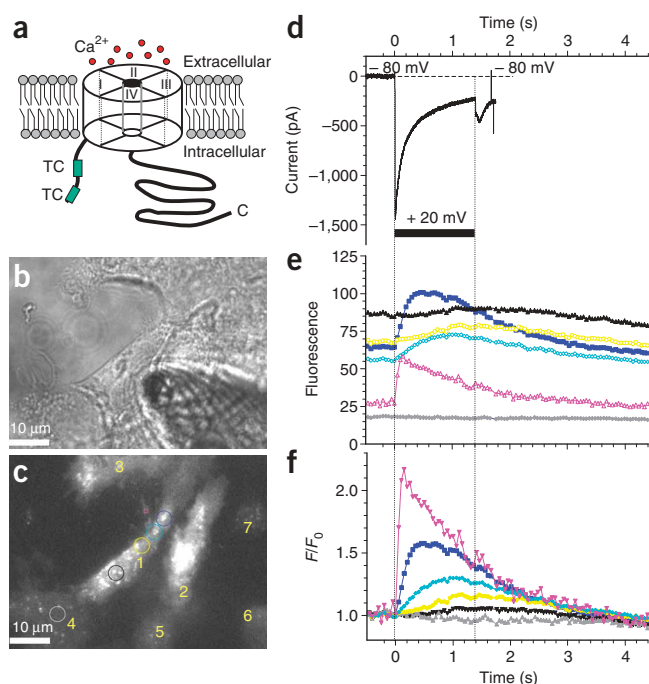
Figure 2 CaGF reports calcium dynamics of L-type calcium channel activation. (**a**) A schematic representation of an α_{1C} channel tagged with two tetracysteine peptides (2TC-α_{1C}). (**b,c**) A typical bright field image of HEK293 cells (**b**) and a TIRF image of the same field following CaGF staining, illustrating seven numbered cells (**c**). Cells 1, 2 and 3 were successfully transfected with the 2TC-α_{1C} construct. Five ROIs are indicated on cell 1 (small magenta ROI, blue, light blue, yellow and black), and one gray ROI is shown on cell 4. (**d**) The membrane potential of cell 1 was clamped at –80 mV and subsequently stepped to +20 mV for 1.4 s. External Ca^{2+} was set at 15 mM and FPL 64176 was added. (**e**) Raw data for CaGF fluorescence is heterogeneous with micron-scale hot spots (magenta and blue) at one end of the cell. (**f**) A plot of F/F_0 illustrates that in this cell the signal rise is fastest and largest at the hot spots.

with 20 μM digitonin (10) and compared fluorescence of gap junctions through a range of imposed calcium concentrations. The fluorescence signal was relatively dim when the cells were bathed in zero calcium plus 1 mM EGTA (11) (**Fig. 1d**) and much brighter in 15 mM calcium (**Fig. 1e**). The fluorescence in six different concentrations of calcium yielded apparent K_d's of 50–61 μM—about half the *in vitro* K_d (**Fig. 1f,g**). This modest discrepancy is probably due to the Donnan potential, the residual potential between the cytosol and the extracellular medium resulting from the net negative charge of the cytosolic macromolecules. A typical Donnan potential of –9 mV (ref. 33) means that when the membrane is permeable to all small ions, intracellular $[Ca^{2+}]$ is twice extracellular $[Ca^{2+}]$, which explains why 50 μM extracellular $[Ca^{2+}]$ suffices to half saturate an indicator with 100 μM K_d. The relative amplitudes of the basal fluorescences versus Ca^{2+}-dependent increments in **Figure 1f** also suggest that practically all the cx43-GFP-C4 molecules have bound CaGF (see **Supplementary Methods** for quantification of completeness of labeling).

To verify that CaGF can report the dynamic of calcium changes in living cells, we elicited calcium waves by using a sharp pipette to poke two cells out of several that are shown in **Supplementary Video 1** online. The cells express cx43-GFP-C4 at localized gap junctions and hemichannels distributed diffusely on the membrane, and they were imaged in high extracellular calcium solution. Two calcium waves that propagate between adjacent cells can be seen in response to the two pokes. The calcium concentrations registered in the impaled cell and its nonimpaled but coupled neighbor were as high as 120 μM and 80 μM at regions adjacent to the gap junction; they gradually decreased to a few micromolar at more distant regions. Notice that our cx43-GFP-C4 continued to conduct Ca^{2+} at concentrations near the upper end of the range reported to close gap junctions[34].

CaGF responses from L-type Ca^{2+} channels are nonuniform

Much previous work has focused on calcium nanodomains around voltage-gated calcium channels. Therefore, we made tetracysteine-tagged α_{1C} L-type calcium channels in order to image local Ca^{2+}

domains near the channel mouths. In contrast to connexin 43, which is highly concentrated and localized at gap junctions, the α_{1C} channels expressed in human embryonic kidney (HEK293) cells are much more difficult to image because of their lower density and more diffuse expression pattern. Therefore, we used total internal reflection fluorescence microscopy (TIRF-M) to improve the signal/background ratio by confining the observation to a thin (~150-nm) section including the plasma membrane, while excluding the majority of intracellular nonspecific background staining (**Supplementary Fig. 1** online). The α_{1C} channels were tagged at the intracellular N terminus either with a tandem repeat of two tetracysteine motifs[35] (2TC-α_{1C}, **Fig. 2**) or with a GFP containing an optimized tetracysteine peptide (N4-GFP-α_{1C}, **Fig. 3**). HEK293 cells stably expressing the β_1 and $\alpha_2\delta$ auxiliary subunits were transiently transfected with the 2TC-α_{1C} construct. **Figure 2a** shows a cartoon of the channel tagged with two tetracysteine motifs. **Figure 2b** depicts a typical bright field image of these cells during patch clamping; **Figure 2c** is a TIRF image of the same field after CaGF staining, illustrating seven numbered cells and six regions of interest (ROIs). Cells 1, 2 and 3 were successfully transfected with the 2TC-α_{1C} constructs: they expressed cotransfected mRFP1 (ref. 36) (data not shown), had a higher CaGF basal signal (**Fig. 2c**), and showed a CaGF fluorescent response. The untransfected cells (cells 4–7) had very low green fluorescent basal counts, no mRFP1, and no CaGF response (**Supplementary Video 2** online).

To activate calcium channels with high temporal precision, we patch clamped individual cells. External Ca^{2+} was set at 15 mM and FPL 64176 (12) was added to the dish to maximize calcium influx[37]. In **Figure 2d**, cell 1 from **Figure 2c** was held at –80 mV and given a 1.4-s depolarizing step to +20 mV (see **Supplementary Fig. 2** online for more details). The current of 1,500 pA is typical; given an expected single-channel conductance[38,39] of 7 pS and driving force of 90 mV, this corresponds to 2,000–2,500 simultaneously open channels.

In a different set of experiments, we estimated the number of channels expressed in transfected cells (N_{cell}) by comparing total fluorescence from confocal reconstructions of cells expressing N4-GFP-α_{1C} with fluorescence from a solution of GFP of known concentration. We also used the confocal images to estimate the fraction of fluorescent signal arising from channels at the plasma membrane ($N_{membrane}$) and found it to be 25–40% of the total signal. To avoid effects from photodamage, we did not patch clamp reconstructed cells, but we used the same criteria to select cells in each case. An alternative and independent method to estimate N_{cell} is to run tens of thousands of cells through a flow cytometer (FACSVantage) and to use a set of fluorescent beads (Bangs Laboratories) with a known number of fluorophores as a fluorescent standard (see **Supplementary Methods** for details on both procedures). Using both methods we found that highly expressing cells had 1–2 million labeled channels on the plasma membrane. Confocal reconstruction of these cells yielded a
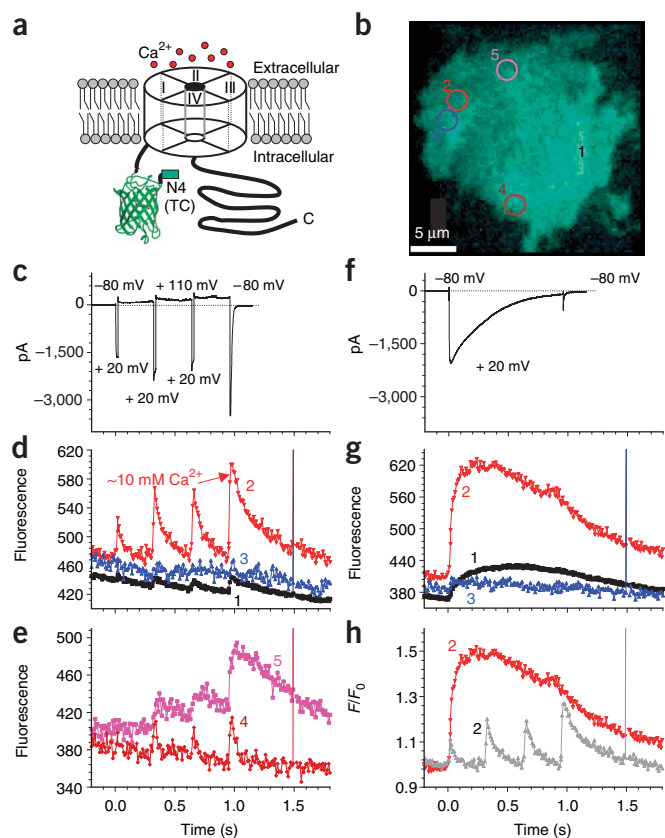
Figure 3 Ca^{2+} transients in response to three 20-ms depolarization pulses. (**a**) A schematic representation of an α_{1C} channel tagged with GFP and the optimized tetracysteine peptide N4 (N4-GFP-α_{1C}). (**b**) A TIRF image showing the locations of the color-coded and numbered ROIs. The black ROI is the entire cell (not shown). (**c**) Current trace with three short depolarization pulses. Time is measured from the beginning of the first pulse. 1 mM BAPTA was present in the pipette; the external solution contains 15 mM Ca^{2+} and 10 µM FPL 64176. (**d**) Three fluorescent traces aligned in time with the current trace. The imaging rate was 100 f.p.s. (**e**) Two additional fluorescent traces registered at ROIs placed on hot spots. (**f**) A second current applied to the same cell, 2 min after the trace shown in **c**, using the protocol of **Figure 2d**. (**g**) Fluorescent signals at the ROI shown in **c** in response to the 960-ms depolarization. (**h**) Comparison of the responses of the red ROI to the two protocols, depicted as F/F_0 (the color of the trace from **d** was switched to gray).

was subsequently induced by application of an ionophore, tearing of the membrane with a sharp pipette, or introducing high concentrations of calcium via the patch pipette (as exemplified in **Supplementary Video 3** online), spatially uniform increases in fluorescence were observed instead. Thus, hot spots are not due to differences in the ability of CaGF to sense calcium or the local density of channels, but rather they reflect stable underlying variations in the probability of channel opening in response to depolarization.

Kinetics and the effects of Ca^{2+} buffering

The calcium signals observed in **Figure 2**, and in similar experiments, are complex in nature. CaGF is expected to be active on open channels, but CaGF should also be activated on closed channels that lie either within the nanodomain of an open channel or in a larger-scale microdomain in which buffers have become saturated and baseline calcium has increased over time. Additionally, a portion of the calcium increase may be caused by release from internal stores, a process known to exist in HEK293 cells[40], and may be triggered by our large α_{1C} calcium influx. Indeed, in a subset of experiments we saw large fluctuations in CaGF signal over hundreds of milliseconds to seconds, which is consistent with slow release from internal stores (data not shown). We therefore refined our experimental protocol in order to maximize the proportion of fluorescent signal from CaGF attached to open channels and reduce the possibility of release from stores. To reduce the time for calcium accumulation, we stepped from –80 mV to +20 mV for 20 ms and then jumped to the calcium reversal potential (+110 mV) to terminate influx and avoid a large tail current. Additional pulses of calcium were delivered by jumping briefly to +20 mV, and a final calcium influx was caused by the tail current when we jumped back to –80 mV. We also changed the calcium buffering in the patch electrode from 4.5 mM EGTA to 1 mM BAPTA; BAPTA is a faster buffer and is therefore more efficient in preventing the spread of Ca^{2+} around open channels. The protocol is diagrammed in detail in **Supplementary Figure 2**.

Figure 3a depicts a schematic representation of an α_{1C} channel tagged with an optimized tetracysteine peptide (N4) and a GFP (N4-GFP-α_{1C}); **Figure 3b** depicts a TIRF image of a cell stably expressing N4-GFP-α_{1C} and also highlights several ROIs on that cell. A typical current trace is provided in **Figure 3c**; peak currents remained in the 1,500–2,000 pA range except for the transient tail current. Three fluorescent traces temporally aligned with the current trace are also shown (**Fig. 3d**; see also **Supplementary Video 4** online). The neighboring red and blue ROIs are a hot spot and a cold spot, respectively, as compared with the whole cell (black ROI). Although the two regions had about the same density of N4-GFP-α_{1C} channels, as indicated by the similar starting fluorescence of all three regions, a

surface area of 1,000–2,000 µm². Thus, transfected cells had a density of approximately 1,000 channels µm⁻². It is important to note the low open probability of these channels even in the presence of FPL 64176: only a few thousand out of several million opened in response to the depolarization stimulus (0.1–0.3% of the total).

During electrical stimulation, fluorescence was simultaneously monitored with TIRF-M (**Fig. 2e,f**). In the example shown, we restricted our analysis to cell 1, which was directly patched. However, cells 2 and 3, which were coupled via endogenous gap junctions to cell 1, showed a complex fluorescent response (**Supplementary Video 2**). The baseline fluorescence of cell 1 was stronger at the center of the cell and gradually became dimmer at the cell's edges. In the simplest case, after depolarization we would expect the highest fluorescent response to be in the region with the highest channel density (yellow and black ROIs). In contrast, as shown in **Figure 2e**, the fluorescent response is heterogeneous with micron-scale hot spots at one end of the cell (magenta and blue ROIs) and no obvious correlation between starting fluorescence and size of response (**Supplementary Video 2**; correlation coefficient $R = -0.1$). A plot of F/F_0 (**Fig. 2f**) illustrates that in this cell the signal rise is fastest and largest at the hot spots at the upper right and decreases in both rate and amplitude downwards and leftwards. The extent of unspecific staining and autofluorescence can be assessed from the signal at nontransfected cells (**Fig. 2c**, cells 4–7 and **Fig. 2e**, gray ROI). Note that in TIRF mode the unspecific staining and autofluorescence signals are low because most of the cell's volume is excluded from the thin imaged layer. The same experimental protocol was repeated three times on this cell with a two-minute interval between repetitions. In each repetition, the same hot spots were activated. Experiments on other cells revealed cell-to-cell variations in the number, location and magnitude of hot spots, but hot spots remained stable within each individual cell. When Ca^{2+} influx
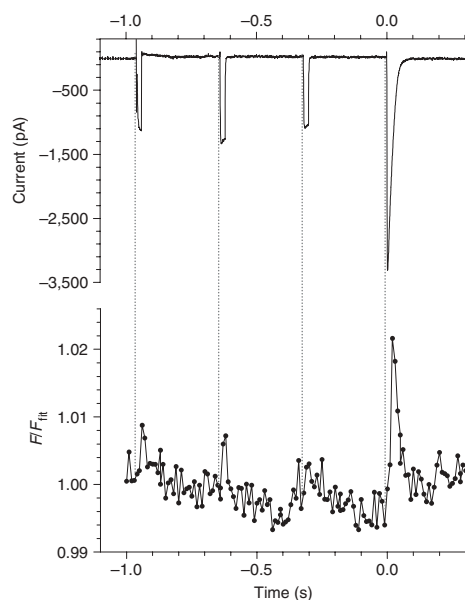
Figure 4 CaGF shows rapid kinetics. The upper panel depicts the current elicited by the same protocol described in **Figure 3c**, except that time was measured from the beginning of the tail current and 40 mM EGTA was present in the patch pipette. Below is the corresponding fluorescent signal, where F/F_{fit} is the photobleaching-corrected signal. The fluorescent response to the tail current (the fourth pulse) is the largest and has almost the same fast time course as the current, which demonstrates the fast K_{off} of CaGF.

spatially heterogeneous calcium response was observed once we depolarized the cell. The relative scarcity of hot spots can be seen in **Supplementary Video 4** and is also exemplified by comparing the red ROI with the black ROI, which encompasses the entire cell and has about one seventh the peak response amplitude of the red signal.

Furthermore, we observed heterogeneous responses at different hot spots. Two additional hot spots (**Fig. 3e**; brown and magenta ROI), as well as the red ROI (**Fig. 3d**), showed a fast rise but differed extensively in the rate of decay. The red and magenta traces were more representative (observed in eight similar experiments) and were surprisingly slow. Because CaGF was engineered to have a fast K_{off}, this slow decay suggests that calcium stays high at these ROIs for tens to hundreds of milliseconds.

To examine whether the hot spots observed with this protocol are the same as those seen previously, we gave one 960-ms depolarization to +20 mV in place of the entire protocol that contained three brief steps. The depolarization elicited a large prolonged calcium current (**Fig. 3f**). The same hot spots continued to show larger fluorescent responses than the cell as a whole, whereas cold spots showed no (or smaller) responses (**Fig. 3g**).

By plotting signals as F/F_0 (**Fig. 3h**) we compared on one graph the signals at the red ROI elicited by two currents (**Fig. 3c,f**). As expected, both protocols gave a similar initial fluorescence increase for the red

ROI hot spot, but the extended stimulation caused a fluorescence peak after approximately 150 ms with a five-fold larger change in fluorescence (**Fig. 3h**). Because the current peak occurred within 20 ms, the extra fluorescence must be due to activation of CaGF bound to closed channels. This confirms that the changes to our protocol reduce the proportion of the signal due to CaGF on closed channels.

If only CaGF bound to open channels were activated, the fluorescence signal would approximately track the current. However, we observed fluorescence that decays more slowly than the current, which suggests that most of the remaining signal was still due to CaGF on closed channels. If the extra signal were caused by local saturation of buffers, increasing the concentration of buffers would reduce the extra signal. A representative recording made with 40 mM EGTA in the pipette is shown in **Figure 4**. Similarly small ($<1\%$ F/F) and fast traces that closely track the calcium current were recorded in all five experiments with 40 mM EGTA in the pipette solution. This result confirms that the slow decays seen in the protocol of **Figure 3c** reflect the underlying calcium dynamics, not an unexpected reduction in the rate of CaGF unbinding.

Modeling of CaGF responses

To better understand these rapid responses, we used a computer model to simulate CaGF activation in the neighborhood of a single open channel (see **Supplementary Methods** for details). In agreement with previous modeling work[10,11,41], we found that a quasi–steady state nanodomain of calcium is established around an open channel within 0.1 ms. The spatial extent of CaGF activation in this nanodomain is limited by its low affinity (**Fig. 5a**, gray line), is restricted still further by 1 mM BAPTA or 40 mM EGTA (**Fig. 5a**, red and black lines, respectively), and is visibly much smaller than the expected activation of a hypothetical dye with a 100-fold higher affinity to calcium (**Fig. 5a**, magenta and cyan). Although the CaGF on the active channel was predicted to be constantly calcium-bound, at observed channel densities of $\sim$1,000 μm^{-2}, we predicted that an average of nine additional CaGFs on nearby closed channels would be active for every one on an open channel. This recruitment of neighboring
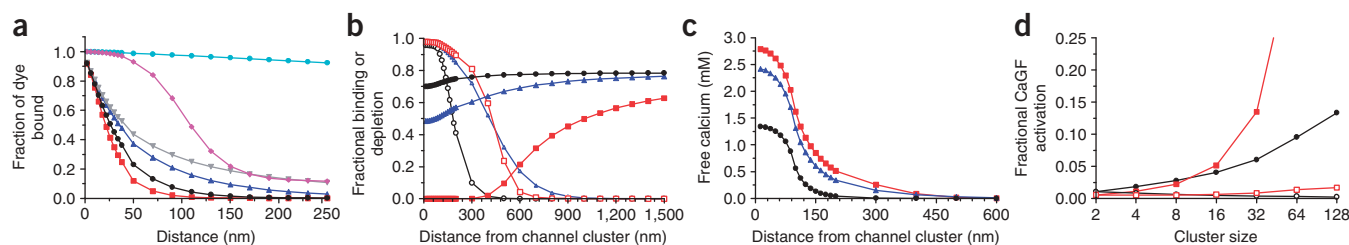
Figure 5 Simulation of CaGF signals. All panels show results after 20 ms of depolarization for 7 pS calcium channels with 100 mV driving force. Channels or clusters of channels are assumed to be uniformly distributed. (**a**) CaGF activated by an isolated open channel. Shown is the predicted fractional activation of CaGF as a function of lateral distance from the channel (red squares, 1 mM BAPTA; black circles, 40 mM EGTA; blue triangles, 4.5 mM EGTA; gray inverted triangles, small-molecule buffers absent) and a hypothetical dye with 100-fold higher affinity (1 mM BAPTA, magenta diamonds; no buffer, cyan circles). (**b**) Fraction of bound CaGF (thin lines, open symbols) and depletion of buffers (thick line, filled symbols) around a cluster of 64 channels; buffers as in **a**. (**c**) Free calcium around a cluster of 64 channels. (**d**) Effect of cluster size. Filled symbols, response in 1-μm hot spot. Open symbols, whole-cell response.

channels is consistent with global fluorescence changes larger than the 0.1–0.3% expected based on the fraction of open channels.

However, the spatial profiles from single-channel modeling (**Fig. 5a**) did not explain the experimentally observed difference in fluorescence between recordings with 40 mM EGTA and those with 1 mM BAPTA (**Fig. 4** and **Fig. 3d,e**, respectively). In particular, these simulations predicted that 1 mM BAPTA would be more efficient than 40 mM EGTA in restricting the spatial extent of CaGF activation. Therefore, we postulated that hot spots were caused by clusters of closely juxtaposed open channels. In simulations of 64 clustered channels, we found that after 20 ms, calcium influx caused depletion of 1 mM BAPTA in half-micron-diameter spots around the channels (**Fig. 5b**), whereas 40 mM EGTA was not exhausted. Under this condition, 40 mM EGTA is substantially more potent in restricting free calcium than 1 mM BAPTA (**Fig. 5c**). To explore this issue further, we plotted the expected fluorescence change as a function of cluster size (**Fig. 5d**). A cluster size of around 32 seemed most consistent with our data: in 1 mM BAPTA, micron-scale hot spots had 5–20% fluorescence changes. Cell-wide changes were ten-fold smaller, and 40 mM EGTA reduced cell-wide changes still further to approximately 0.5%; these values are within the observed ranges (**Fig. 3d,e** and **Fig. 4**). These numbers are not definitive, as we only tested the extremes of uniform and highly clustered active channels; the exact values also depend on the distribution of inactive channels, assumed here to be uniform. Nonetheless, the model broadly agrees with our interpretation of the fluorescence data and suggests that hot spots consist of a few dozen responsive channels in an area of a square micron or two.

DISCUSSION

Calcium nanodomains—spatially and temporally restricted regions of high calcium—are important for a variety of biological processes[1,2]. However, they are difficult to observe directly because they are too small to resolve optically, and because they are established and decay quickly. CaGF has several attractive features for studying calcium nanodomains. First, CaGF can be genetically targeted to bind specifically to a protein of interest in order to provide a readout of the calcium environment of that protein. Second, the impact on the targeted protein is minimal, as the binding peptide is short and CaGF itself is small. Third, CaGF has rapid kinetics that can track changes in calcium concentration on the millisecond timescale. Fourth, CaGF has a relatively low affinity and therefore is highly activated in only a small neighborhood of a calcium source. CaGF therefore has the potential to provide information about spatial structure below optical resolution.

We have demonstrated highly specific labeling of target proteins with CaGF, used CaGF to directly visualize micron-scale hot spots of calcium influx (calcium microdomains), and inferred the existence of calcium domains of hundreds of nanometers from simulations and from the time course of CaGF fluorescence under conditions in which individual spots could not be resolved optically. Note that the tagging of a reporter to a target protein is necessary but not sufficient in order to register a nanodomain signal. It is also necessary for the signal to form a nanodomain of significantly higher concentration than elsewhere, for the protein to be located within that nanodomain, and for the reporter to be selectively activated in that concentration range. In particular, tagging a calcium channel with CaGF does not automatically create a reporter that is activated if and only if the calcium channel is open. In our case, even with high buffer concentrations, experiments and simulations suggested that only ~10–30% of our signal was from CaGF bound to open channels (with higher values for more clustered channels). Thus, because of the large number of closed,

unresponsive channels present on the plasma membrane, CaGF functioned primarily as a membrane-associated calcium indicator. However, our results indicate that CaGF has the desired kinetics, affinity and specificity for probing nanodomains.

It is tempting to try to report a value for calcium concentration. However, unlike with conventional calcium imaging, in which the calcium concentration is usually assumed to be approximately uniform within a spot of optical resolution, we are specifically interested in situations in which concentrations vary widely. A fluorescence response in our experiments is expected to be a complex mixture arising from fully saturated CaGF near the source as well as infrequent binding of Ca^{2+} to CaGF further away, all within the limits of optical resolution. In principle, comparison between observations and simulations could yield quantitative information about the extent and magnitude of calcium nanodomains as long as calcium sources are widely separated. Unfortunately we found strong clustering of calcium sources, which left us unable to quantitatively measure nanodomains. Nonetheless, if CaGF is bound to a Ca^{2+} source such as a channel, or a calcium-sensitive protein, the total response is a meaningful measure of the biological impact of the calcium transient on that protein, at least if the protein has an affinity for calcium in the range in which CaGF is sensitive. Therefore, the difficulty in assigning a single number to calcium concentration does not prevent assignment of biological relevance.

With lower concentrations of buffers, we observed micron-scale hot spots and cold spots of calcium even though channel density appeared approximately uniform, at least within optical resolution. What might cause this spatial nonuniformity? Extracellular depletion of calcium between the cell membrane and the coverslip is not likely to account for the observations, at least for short depolarizations, as simulations predict that depletion is likely to be modest (see **Supplementary Methods** for details). Additionally, if hot spots were the result of large extracellular pockets, the resting fluorescence in TIRF should be dim at hot spots owing to the extra distance to the membrane and coverslip; we do not observe this. It is also unlikely that the intracellular space is sufficiently constrained to cause local calcium buildup, given that we observe hot spots across the bottom face of the cell, not just at the edges, where diffusion may be constrained. Profound heterogeneity in endogenous buffer distribution may have some role, but because hot spots remain during extended depolarizations that should exhaust any endogenous buffers, this cannot explain the majority of the effect. We cannot entirely rule out the possibility that hot spots result from release from intracellular stores, although two lines of evidence argue against this. First, in a subset of experiments with low calcium buffering, we observed slow, variable calcium responses suggestive of intracellular release. Second, imaging in 40 mM EGTA revealed transients that were more tightly coupled to the currents than would be expected by any known intracellular release mechanism, which indicates that under those conditions, most of the current is not from intracellular stores. Thus, at least for the rising phase of the calcium transients, the most likely cause of hot spots is nonuniform distribution of responsive channels. Consistent with this idea, most channels remain closed even during depolarization in high calcium with FPL 64176, which suggests that most channels have been deactivated. Furthermore, models of calcium influx are consistent with hot spots consisting of a few dozen highly clustered activated channels. Thus, our data suggest that hot spots are small regions where responsive channels are present at higher density, and that most channels are essentially nonresponsive.

Other reports suggest the existence of regions of highly localized activated calcium channels. L-type Ca^{2+} channels have a rather

uniform distribution in arterial myocytes, but highly localized and clustered protein kinase C activates clusters of L-type Ca^{2+} channels that give rise to Ca^{2+} sparklets[42]. This example of hot spots induced by phosphorylation suggests that a similar process may occur in our system, and it is consistent with the idea that in our system, most of the channels are kept silent, and hot spots are caused by a local release from inhibition.

The large fraction of silent channels in our HEK293 expression system persisted despite our best efforts to increase the open probability. First, we used a cell line stably expressing the β_4 and $\alpha_2\delta$ auxiliary subunits[43] that in addition was transiently transfected with the β_1 subunit, all of which gave about a two-fold increase in P_{open}. Second, the potent drug FPL 64176 was applied[37], and as expected, a variable increase of about five-fold was observed. We also tried to grow the cells in the presence of 10 μM nifedipine (13) in order to try to prevent a negative selection, due to calcium cytotoxicity, against cells expressing more channels. This treatment had no apparent effect on P_{open}. Taken together, all these measures did result in an ~ten-fold increase in the P_{open} of L-type channels, but even after this increase average P_{open} remained well below 0.01.

Others have reported very low P_{open} of L-type channels. One group[44] recorded single channels from *Xenopus laevis* oocytes and found P_{open} to be as low as 0.0001, which increased to about 0.003 when the α_{1C} subunit was coexpressed with both the β and $\alpha_2\delta$ auxiliary subunits. Their method could not detect channels that were completely silent, so the actual P_{open} might have been even lower. In our case, the reproducibility of hot spots demonstrates that P_{open} is high for a responsive subset of channels; we cannot estimate how small P_{open} is for nonresponsive channels, or how many distinct states of different responsiveness the channels can adopt.

In addition to the nonuniform open probability leading to hot spots, we also observed variability in the rate of return to baseline for calcium signals. A variety of factors could be responsible. A region of interest placed away from the peak density would show slower rises because calcium would take more time to diffuse there and saturate buffers in that area. Large hot spots might show a slower decay of the response because unbound buffers would have farther to diffuse to remove excess calcium. However, there may be other relevant factors that are not related to the local density of activated channels. Low-affinity immobile endogenous buffers could locally alter the effective calcium diffusion constant by holding Ca^{2+} immobile for a significant fraction of the time in regions with high buffer concentration. Additionally, calcium pumps could be concentrated in some areas and not others, causing faster decays and lower peaks in areas with a high concentration of pumps. At this point, it is difficult to distinguish between these different hypotheses.

A variety of direct applications of CaGF, beyond those presented here, are possible. For example, CaGF could be used to monitor the calcium environment of various presynaptic and postsynaptic calcium-sensitive proteins, such as synaptotagmin and presynaptic calcium channels. Furthermore, it will be advantageous to study systems in which these proteins are expressed endogenously and participate in physiological processes, such as at the large presynaptic calyx of Held. Measurement of CaGF signal could provide a qualitative and possibly quantitative answer to whether nanodomains are important for the function of a given protein. This approach is complementary to inference from experiments in which buffer concentrations are altered; the latter can be used to manipulate nanodomains, whereas the former reports the calcium environment. Alternatively, in systems with lower densities of calcium channels (tens to hundreds per square micron, depending on buffering and the conductance of the channel) and a

larger average P_{open}, CaGF could be used as a direct reporter of calcium channel state. Reducing the already small signal we observed by an additional factor of ten or more might seem daunting, but combining averaging with a GFP-free system, multiple CaGF tags per channel and a further increase in the channel open probability should all promote a better signal-to-noise ratio than we observed (**Fig. 4**). In such experiments it will be important to keep nonspecific CaGF labeling to a minimum. Also, with low baseline fluorescence, autofluorescence may make measurements of fractional intensity change unreliable. However, calibration can still be achieved by imposing zero-calcium and high-calcium conditions at the end of each experiment.

Imaging with CaGF can also be combined with conventional calcium imaging techniques. Because CaGF response depends strongly on distance from a calcium source, clustering of calcium sources and target proteins on the molecular scale, such as in rafts, would produce a large response compared with that from uniformly distributed targets. CaGF response also depends strongly on calcium influx, but a second cytosolic indicator with a noninterfering excitation/emission spectrum could be used to provide an independent measure of calcium influx. Thus, paired recordings could provide a quantitative measure of clustering or localization beyond the simple yes/no results that can be attained with CaGF alone.

METHODS

Gene construction. cx43-TC and 2TC-α_{1C} were previously described[28,35]. The 4N-Emerald-α_{1C} clone was constructed by annealing sense and antisense DNAs encoding the 4N tetracysteine[32] GSFLNCCPGCCMEPGGR, where GS and GGR amino acids are translated from *Bam*HI and *Not*I restriction-site nucleotides, respectively. The 4N tetracysteine was subcloned to the N terminus of Emerald GFP and to the N terminus of the α_{1C}, up to the endogenous *Cla*I site in the full-length α_{1C}. The 4N-Emerald-α_{1C} fragment was ligated into the α_{1C} pCDNA3 (Invitrogen) plasmid and digested with *Hin*dIII and *Cla*I. The cloned product was sequenced to ensure fidelity and amplified in DH5α *Escherichia coli*. The cx43–Emerald GFP–4C was constructed as follows: a modified pCLNCX vector containing Emerald GFP–4C (ref. 32) was cut with *Hin*dIII and *Bam*HI and ligated to the digested PCR product of cx43 (5′-GGGA AGCTTGCCACCATGGGTGACTGGAGTGCCTTGGGGAAATTACTGGACAA GGCCCCGGATCCACTGCTCTCAATCTCCAGGTCATCAGGCCG-3′). Retrovirus was generated by cotransfection with pCL-Ampho (Imgenex), filtered and transduced to the cells in the presence of 8 μg ml^{-1} polybrene.

Cell culture. Intercellular communication–deficient, cx43-negative HeLa cells (for cx43 experiments) or HEK293 cells stably expressing β_1 and $\alpha_2\delta$ (stable HEK293; ref. 43) (for α_{1C} experiments) were seeded onto 35-mm Petri dishes with glass windows, in DMEM supplemented with 10% FBS and 1% penicillin/streptomycin (enriched DMEM). The stable HEK293 were maintained with 600 ng ml^{-1} of G418 (Invitrogen). The cells were grown for 24 h to about 40% confluence, transiently transfected using FuGENE 6 (Roche Diagnostics) and examined 24 to 48 h after transfection. For some experiments involving patch clamping of α_{1C} channels, we preferred patching single cells rather than one cell from a cluster because the voltage clamp and the current interpretation were simpler. Therefore, 24 h after transfection the cells were lifted, diluted and reseeded on imaging dishes with less then 5% confluence in order to easily find single cells. HeLa cells were transfected with 1 μg of cx43-TC or cx43-GFP-TC constructs. Stable HEK293 cells for the β_1 and $\alpha_2\delta$ subunits were transiently cotransfected with 2 μg of the various α_{1C} constructs together with 1 μg of β_4 constructs.

CaGF labeling. The AM ester form of CaGF (1–4 μM final concentration) was premixed with EDT (10 μM), added to the imaging dishes and kept in a 37 °C incubator in enriched DMEM for various periods of time (4 to 24 h) before the imaging experiment. To increase the solubility of CaGF, the 1–2 μl CaGF stock solution was also premixed with 1 μl of Pluronic F-127 (20%) in DMSO solution and 300 μl of enriched DMEM solution before addition to the dish.

After CaGF labeling and before performing of the experiments, excess dye was quenched by a 10-min wash with 250 μM EDT in our extracellular bath solutions.

Electrophysiology. Cells were voltage clamped with a patch clamp amplifier (Axopatch-200B, Molecular Devices), and depolarizing steps were applied to induce calcium currents. The bath solution contained (in mM) 160 tetraethylammonium (TEA)-Cl, 10 $CaCl_2$, 10 HEPES and CsOH to give a pH of 7.3, and the pipette contained 108 $CsMeSO_4$, 4.5 $MgCl_2$, 4.5 EGTA, 4.5 Na_2ATP, 0.3 Na_3GTP, 24 HEPES, and CsOH to give a pH of 7.3. The 4.5 EGTA was replaced by 1 mM BAPTA in one subset of experiments; in another subset 40 mM EGTA was used together with reduction of the $CsMeSO_4$ concentration from 108 mM to 72 mM to keep the osmolarity at 305 mosM.

Currents were digitized and analyzed with Digidata 1200B and pCLAMP8.1 software (Molecular Devices). The ensemble whole-cell macroscopic currents had similar amplitudes, kinetics, voltage sensitivity and pharmacological sensitivity regardless of whether cells had untagged α_{1C} channels, tagged α_{1C} channels without CaGF, or tagged α_{1C} channels following CaGF labeling (see also **Supplementary Fig. 3** online). This agrees with previous work showing that linking of GFP to the N terminus of α_{1C} channels has no effect on current[45]. Cells selected for patching appeared healthy under transmitted light and were in the brightest 25% under widefield fluorescence; the brightest and dimmest cells we selected varied in intensity by a factor of less than two.

TIRF-M. Images were acquired using a through-the-lens Olympus IX71 TIRF microscope equipped with either a PlanApo ×60, 1.45 numerical aperture lens, or an Apo ×100, 1.65 numerical aperture lens. In the latter case, a special immersion medium of high refractive index $n(d) = 1.78$ (Cargille Laboratories) was used along with a special coverslip glass with a high refractive index ($n(d) = 1.788$; Olympus). Illumination was provided by a 488 ion laser (Melles Griot). Images were acquired using a Cascade 512B CCD camera with the camera gain set at 2× (Photometrics); images were streamed and analyzed using MetaFluor software (Molecular Devices). Interference filters and dichroic mirrors were from Chroma. MetaFluor was used to quantify fluorescence in regions of interest. Figures show average intensity minus average background fluorescence in all traces except those with 40 mM EGTA. Because of the small nature of this signal, baseline camera counts, bleaching and background fluorescence were accounted for by first fitting the raw data trace by a single exponent ($R^2 = 0.9999$); then the fluorescent trace was divided by the fit (F/F_{fit}) to generate a bleaching-corrected trace.

Note: Supplementary information and chemical compound information is available on the Nature Chemical Biology website.

AUTHOR CONTRIBUTIONS
S.R.A. and R.Y.T. designed CaGF. S.R.A. synthesized and characterized CaGF. O.T. and R.Y.T. designed the connexin 43 experiments. O.T., R.W.T. and R.Y.T. designed the calcium channel experiments. R.W.T. provided the α1C cDNA and cell line expressing the other Ca2+ channel subunits. O.T. and R.M.M. created the constructs and final cell lines, and O.T. performed the imaging, electrophysiology and data analysis. R.A.K. and T.J.S. designed the simulations and R.A.K. implemented them. O.T., S.R.A., R.A.K. and R.Y.T. prepared the manuscript.

COMPETING INTERESTS STATEMENT
The authors declare competing financial interests: details accompany the full-text HTML version of the paper at www.nature.com/naturechemicalbiology/.

Published online at http://www.nature.com/naturechemicalbiology
Reprints and permissions information is available online at http://npg.nature.com/reprintsandpermissions

1. Augustine, G.J., Santamaria, F. & Tanaka, K. Local calcium signaling in neurons. *Neuron* **40**, 331–346 (2003).
2. Rizzuto, R. & Pozzan, T. Microdomains of intracellular Ca^{2+}: molecular determinants and functional consequences. *Physiol. Rev.* **86**, 369–408 (2006).
3. Yamada, W.M. & Zucker, R.S. Time course of transmitter release calculated from simulations of a calcium diffusion model. *Biophys. J.* **61**, 671–682 (1992).
4. Parnas, H., Segel, L., Dudel, J. & Parnas, I. Autoreceptors, membrane potential and the regulation of transmitter release. *Trends Neurosci.* **23**, 60–68 (2000).
5. Llinás, R., Sugimori, M. & Silver, R.B. Microdomains of high calcium concentration in a presynaptic terminal. *Science* **256**, 677–679 (1992).
6. Aharon, S., Bercovier, M. & Parnas, H. Parallel computation enables precise description of Ca^{2+} distribution in nerve terminals. *Bull. Math. Biol.* **58**, 1075–1097 (1996).
7. Sugimori, M., Lang, E.J., Silver, R.B. & Llinas, R. High-resolution measurement of the time course of calcium-concentration microdomains at squid presynaptic terminals. *Biol. Bull.* **187**, 300–303 (1994).
8. Marsault, R., Murgia, M., Pozzan, T. & Rizzuto, R. Domains of high Ca^{2+} beneath the plasma membrane of living A7r5 cells. *EMBO J.* **16**, 1575–1581 (1997).
9. Schneggenburger, R. & Neher, E. Intracellular calcium dependence of transmitter release rates at a fast central synapse. *Nature* **406**, 889–893 (2000).
10. Simon, S.M. & Llinas, R.R. Compartmentalization of submembrane calcium activity during calcium influx and its significance in transmitter release. *Biophys. J.* **48**, 485–498 (1985).
11. Naraghi, M. & Neher, E. Linearized buffered Ca^{2+} diffusion in microdomains and its implications for $[Ca^{2+}]$ at the mouth of a calcium channel. *J. Neurosci.* **17**, 6961–6973 (1997).
12. Stanley, E.F. Single calcium channels and acetylcholine release at a presynaptic nerve terminal. *Neuron* **11**, 1007–1011 (1993).
13. Borst, J.G.G. & Sakmann, B. Calcium current during a single action potential in a large presynaptic terminal of the rat brainstem. *J. Physiol. (Lond.)* **506**, 143–157 (1998).
14. DiGregorio, D.A., Peskoff, A. & Vergara, J.L. Measurement of action potential-induced presynaptic calcium domains at a cultured neuromuscular junction. *J. Neurosci.* **19**, 7846–7859 (1999).
15. Zou, H., Lifshitz, L.M., Tuft, R.A., Fogarty, K.E. & Singer, J.J. Imaging Ca^{2+} entering the cytoplasm through a single opening of a plasma membrane cation channel. *J. Gen. Physiol.* **114**, 575–588 (1999).
16. Zenisek, D., Davila, V., Wan, L. & Almers, W. Imaging calcium entry sites and ribbon structures in two presynaptic cells. *J. Neurosci.* **23**, 2538–2548 (2003).
17. Demuro, A. & Parker, I. "Optical patch-clamping": single-channel recording by imaging Ca^{2+} flux through individual muscle acetylcholine receptor channels. *J. Gen. Physiol.* **126**, 179–192 (2005).
18. Rizzuto, R., Simpson, A.W., Brini, M. & Pozzan, T. Rapid changes of mitochondrial Ca^{2+} revealed by specifically targeted recombinant aequorin. *Nature* **358**, 325–327 (1992).
19. Brini, M. *et al.* Nuclear Ca^{2+} concentration measured with specifically targeted recombinant aequorin. *EMBO J.* **12**, 4813–4819 (1993).
20. Montero, M. *et al.* Monitoring dynamic changes in free Ca^{2+} concentration in the endoplasmic reticulum of intact cells. *EMBO J.* **14**, 5467–5475 (1995).
21. Miyawaki, A. *et al.* Fluorescent indicators for Ca^{2+} based on green fluorescent proteins and calmodulin. *Nature* **388**, 882–887 (1997).
22. Palmer, A.E., Jin, C., Reed, J.C. & Tsien, R.Y. Bcl-2-mediated alterations in endoplasmic reticulum Ca^{2+} analyzed with an improved genetically encoded fluorescent sensor. *Proc. Natl. Acad. Sci. USA* **101**, 17404–17409 (2004).
23. Palmer, A.E. *et al.* Ca^{2+} indicators based on computationally redesigned calmodulin-Peptide pairs. *Chem. Biol.* **13**, 521–530 (2006).
24. Mank, M. *et al.* A FRET-based calcium biosensor with fast signal kinetics and high fluorescence change. *Biophys. J.* **90**, 1790–1796 (2006).
25. Lee, M.Y. *et al.* Local subplasma membrane Ca^{2+} signals detected by a tethered Ca^{2+} sensor. *Proc. Natl. Acad. Sci. USA* **103**, 13232–13237 (2006).
26. Griffin, B.A., Adams, S.R. & Tsien, R.Y. Specific covalent labeling of recombinant protein molecules inside live cells. *Science* **281**, 269–272 (1998).
27. Adams, S.R. *et al.* New biarsenical ligands and tetracysteine motifs for protein labeling *in vitro* and *in vivo*: synthesis and biological applications. *J. Am. Chem. Soc.* **124**, 6063–6076 (2002).
28. Gaietta, G. *et al.* Multicolor and electron microscopic imaging of connexin trafficking. *Science* **296**, 503–507 (2002).
29. Kuhn, M.A. in *Fluorescent Chemosensors for Ion and Molecule Recognition* (ed. Czarnik, A.W.) 147–161 (American Chemical Society, Washington, DC, 1993).
30. Levy, L.A., Murphy, E., Raju, B. & London, R.E. Measurement of cytosolic free magnesium ion concentration by 19F NMR. *Biochemistry* **27**, 4041–4048 (1988).

31. Naraghi, M. T-jump study of calcium binding kinetics of calcium chelators. *Cell Calcium* **22**, 255–268 (1997).
32. Martin, B.R., Giepmans, B.N., Adams, S.R. & Tsien, R.Y. Mammalian cell-based optimization of the biarsenical-binding tetracysteine motif for improved fluorescence and affinity. *Nat. Biotechnol.* **23**, 1308–1314 (2005).
33. Regini, J.W. & Elliott, G.F. The effect of temperature on the Donnan potentials in biological polyelectrolyte gels: cornea and striated muscle. *Int. J. Biol. Macromol.* **28**, 245–254 (2001).
34. Peracchia, C. Chemical gating of gap junction channels; roles of calcium, pH and calmodulin. *Biochim. Biophys. Acta* **1662**, 61–80 (2004).
35. Tour, O., Meijer, R.M., Zacharias, D.A., Adams, S.R. & Tsien, R.Y. Genetically targeted chromophore-assisted light inactivation. *Nat. Biotechnol.* **21**, 1505–1508 (2003).
36. Campbell, R.E. *et al.* A monomeric red fluorescent protein. *Proc. Natl. Acad. Sci. USA* **99**, 7877–7882 (2002).
37. Rampe, D. & Lacerda, A.E. A new site for the activation of cardiac calcium channels defined by the nondihydropyridine FPL 64176. *J. Pharmacol. Exp. Ther.* **259**, 982–987 (1991).
38. Church, P.J. & Stanley, E.F. Single L-type calcium channel conductance with physiological levels of calcium in chick ciliary ganglion neurons. *J. Physiol. (Lond.)* **496**, 59–68 (1996).
39. Guia, A., Stern, M.D., Lakatta, E.G. & Josephson, I.R. Ion concentration-dependence of rat cardiac unitary L-type calcium channel conductance. *Biophys. J.* **80**, 2742–2750 (2001).
40. Luo, D., Sun, H., Xiao, R.P. & Han, Q. Caffeine induced Ca^{2+} release and capacitative Ca^{2+} entry in human embryonic kidney (HEK293) cells. *Eur. J. Pharmacol.* **509**, 109–115 (2005).
41. Shuai, J. & Parker, I. Optical single-channel recording by imaging Ca^{2+} flux through individual ion channels: theoretical considerations and limits to resolution. *Cell Calcium* **37**, 283–299 (2005).
42. Navedo, M.F. *et al.* Constitutively active L-type Ca^{2+} channels. *Proc. Natl. Acad. Sci. USA* **102**, 11112–11117 (2005).
43. Piedras-Renteria, E.S. *et al.* Increased expression of alpha(1A) Ca^{2+} channel currents arising from expanded trinucleotide repeats in spinocerebellar ataxia type 6. *J. Neurosci.* **21**, 9185–9193 (2001).
44. Shistik, E., Ivanina, T., Puri, T., Hosey, M. & Dascal, N. Ca^{2+} current enhancement by α2/δ and β subunits in *Xenopus* oocytes: contribution of changes in channel gating and α1 protein level. *J. Physiol. (Lond.)* **489**, 55–62 (1995).
45. Grabner, M., Dirksen, R.T. & Beam, K.G. Tagging with green fluorescent protein reveals a distinct subcellular distribution of L-type and non-L-type Ca^{2+} channels expressed in dysgenic myotubes. *Proc. Natl. Acad. Sci. USA* **95**, 1903–1908 (1998).